



Cite this: *Chem. Sci.*, 2022, **13**, 11639

All publication charges for this article have been paid for by the Royal Society of Chemistry

## Understanding the electrocatalytic mechanism of self-template formation of hierarchical $\text{Co}_9\text{S}_8/\text{Ni}_3\text{S}_2$ heterojunctions for highly selective electroreduction of nitrobenzene<sup>†</sup>

Xuanping Wang,<sup>‡a</sup> Longbin Li,<sup>‡ab</sup> Mingzhu Shi,<sup>a</sup> Yiqi Wang,<sup>c</sup> Guodong Xu,<sup>a</sup> Kai Yuan, Peipei Zhu,<sup>\*a</sup> Mengning Ding <sup>\*ac</sup> and Yiwang Chen <sup>\*ab</sup>

Aqueous electrochemical nitroarene reduction reaction using  $\text{H}_2\text{O}$  as the sustainable hydrogen source is an emerging technology to produce functionalized anilines. However, the development of low-cost electrocatalysts and the fundamental mechanistic understanding of the selective NO-RR still remain challenging. Herein, self-supporting hierarchical nanosheets consisting of high-density  $\text{Co}_9\text{S}_8/\text{Ni}_3\text{S}_2$  heterojunctions on Ni foam ( $\text{Co}_9\text{S}_8/\text{Ni}_3\text{S}_2$ -NF) are constructed *via* an *in situ* self-template strategy. With combined advantages of high-loading, high surface exposure, efficient conductivity and unique electronic structure of the  $\text{Co}_9\text{S}_8/\text{Ni}_3\text{S}_2$  interface, the as-prepared  $\text{Co}_9\text{S}_8/\text{Ni}_3\text{S}_2$ -NF exhibits efficient electrocatalytic NO-RR performance, including up to 99.0% conversion and 96.0% selectivity towards aniline, and outstanding functional group tolerance. Mechanistic investigations and theoretical calculations reveal that electron transfer from  $\text{Ni}_3\text{S}_2$  to  $\text{Co}_9\text{S}_8$  is beneficial for the co-adsorption of  $\text{H}_2\text{O}$  and nitrobenzene molecules at the interfacial sites, promoting the formation of active hydrogen and subsequent reduction of nitrobenzene. Additionally, the interfacial charge transfer breaks the symmetry of two active Co sites at the  $\text{Co}_9\text{S}_8/\text{Ni}_3\text{S}_2$  interface, which markedly reduces the energy barrier for reduction of nitrobenzene to aniline. This work offers a successful example for the interfacial engineering of metal sulfide-based heterojunctions with excellent electrocatalytic nitroarene reduction performance, and also paves the way for the in-depth understanding of the corresponding mechanism.

Received 27th June 2022  
Accepted 17th September 2022

DOI: 10.1039/d2sc03585e  
[rsc.li/chemical-science](http://rsc.li/chemical-science)

## Introduction

Functionalized aniline ( $\text{PhNH}_2$ ) is a group of vital chemical stocks in many industries, including dye, drug, conductive polymer, transparent electrode and pseudocapacitor.<sup>1–3</sup> Traditional  $\text{PhNH}_2$  production *via* thermocatalytic or direct-amination endures the issues of high energy consumption, high carbon emission, high cost and unsafe proton donors (Table S1<sup>†</sup>).<sup>4–9</sup> In addition, current nitroarene reduction reactions (NO-RR) typically utilize rare noble metals (Pt, Pd, Ru, Rh,

etc.) as catalysts, which however face a significant challenge in achieving satisfactory chemoselectivity and are vulnerable to functional group poisoning.<sup>10–12</sup> Moreover, the harsh reaction conditions lead to low compatibility with fragile groups ( $-\text{OCH}_3$ ,  $-\text{OH}$ ,  $-\text{Cl}$ ,  $-\text{F}$ ,  $-\text{Br}$ , or/and  $-\text{COCH}_3$ , etc.), which severely limits the scope of substrates for NO-RR.<sup>2,13–16</sup> Therefore, it is crucial to develop noble-metal-free catalysts that enable selective reduction of functionalized nitroarenes with fragile side groups under mild conditions. In recent years, electrochemical organic synthesis has inspired the field with multiple advantages including ambient reaction conditions, utilization of sustainable electrical energy, and controllable selectivity.<sup>17–20</sup> With continuous efforts, electrocatalytic nitroarene reduction has been greatly promoted, especially *via* the development of high-performance electrocatalysts (Table S2<sup>†</sup>) into the most promising technology for  $\text{PhNH}_2$  production.<sup>2,13,15,16,21,22</sup> However, few studies uncover the active origins and fundamental mechanism of the selective NO-RR process under aqueous conditions.

In view that reactive hydrogen ( $\text{H}^*$ ) participates and plays a crucial role in the aqueous electrochemical NO-RR,  $\text{H}_2\text{O}$  activation performance of NO-RR electrocatalysts should be carefully considered for the modulation of their activities.<sup>13,15</sup>

<sup>a</sup>National Engineering Research Center for Carbohydrate Synthesis, Key Lab of Fluorine and Silicon for Energy Materials and Chemistry of Ministry of Education, College of Chemistry and Chemical Engineering, Jiangxi Normal University, 99 Ziyang Avenue, Nanchang 330022, China. E-mail: [ppzhu@jxnu.edu.cn](mailto:ppzhu@jxnu.edu.cn); [mding@jnu.edu.cn](mailto:mding@jnu.edu.cn); [ywchen@ncu.edu.cn](mailto:ywchen@ncu.edu.cn)

<sup>b</sup>Institute of Polymers and Energy Chemistry (IPEC), Nanchang University, 999 Xuefu Avenue, Nanchang 330031, China

<sup>c</sup>Key Laboratory of Mesoscopic Chemistry, School of Chemistry and Chemical Engineering, Nanjing University, 163 Xianlin Avenue, Nanjing 210023, China

<sup>†</sup> Electronic supplementary information (ESI) available. See <https://doi.org/10.1039/d2sc03585e>

<sup>‡</sup> These authors contributed equally.



Previous studies have confirmed that highly conductive transition metal sulfides (TMSs) with favorable  $\text{H}_2\text{O}$  adsorption show promising potential in  $\text{H}_2\text{O}$  splitting to replace precious metals.<sup>23–31</sup> Nevertheless, pure TMSs exhibit weak adsorption on nitrobenzene ( $\text{PhNO}_2$ ), which leads to premature desorption of  $\text{PhNO}_2$  on the catalyst surface, leading to insufficient and incomplete reduction to  $\text{PhNH}_2$ .<sup>15</sup> To this end, interface engineering is an efficient strategy towards electronic structure regulation of interfacial active sites for designing efficient electrocatalysts.<sup>23,27,32–35</sup> For example, Fu *et al.* successfully fabricated a  $\text{MoO}_2$ –FeP heterojunction for efficient electrochemical hydrogen evolution and 5-HMF reaction, and interfacial electron redistribution between  $\text{MoO}_2$ –FeP was confirmed as the origin of enhanced activity.<sup>23</sup> In addition to the electronic structure, reasonable geometry regulations including the microstructure of electrocatalysts and selection of substrates are of vital importance.<sup>36–38</sup> Construction of anisotropic nanosheets on conductive substrates can also increase active site exposure, accelerate mass transfer, and improve the electrical conductivity of electrocatalysts.<sup>39,40</sup>

Herein, self-supporting hierarchical nanosheets composed of  $\text{Co}_9\text{S}_8/\text{Ni}_3\text{S}_2$  heterojunctions were constructed on Ni foam ( $\text{Co}_9\text{S}_8/\text{Ni}_3\text{S}_2$ –NF), with unique and abundant active interfaces that promote hydrogenation and conversion of nitroarenes into functionalized  $\text{PhNH}_2$ . The as-prepared  $\text{Co}_9\text{S}_8/\text{Ni}_3\text{S}_2$ –NF shows efficient electrocatalytic reduction of  $\text{PhNO}_2$  to  $\text{PhNH}_2$  with up to 99.0% conversion and 96.0% selectivity under alkaline conditions, and demonstrates NO-RR favorable functional group tolerance. Both theoretical calculations and experimental characterization identify the critical role of electron transfer from  $\text{Ni}_3\text{S}_2$  to  $\text{Co}_9\text{S}_8$ , which favors  $\text{H}_2\text{O}$  activation for the formation of  $\text{H}^*$  and adsorption of  $\text{PhNO}_2$  onto Co sites, thus improving the NO-RR activity. This work offers a design principle for NO-RR electrocatalysts *via* low-cost TMS-based heterojunction engineering, and also provides a systematic understanding of the electrocatalytic reduction mechanism during NO-RR.

## Results and discussion

The construction of  $\text{Co}_9\text{S}_8/\text{Ni}_3\text{S}_2$ –NF was achieved by *in situ* sulfuration of Co–Ni layered-double-hydroxide (LDH) precursors pre-formed on the Ni foam (CoNi-LDH/NF) (Fig. 1a). First, CoNi-LDH/NF was prepared by a hydrothermal method with the Ni foam substrate placed in the Co salt and urea precursor solution at 120 °C. Subsequently, *in situ* sulfuration of self-sacrificing CoNi-LDH/NF was conducted by a second hydrothermal process with  $\text{Na}_2\text{S}$  as the S source under 160 °C, and the final  $\text{Co}_9\text{S}_8/\text{Ni}_3\text{S}_2$ –NF was obtained. For better control of the morphology and catalytic performance of CoNi-LDH/NF precursors, the optimized hydrothermal time and the ratio of Co salts to urea is 8 hours and 1 : 1, respectively. For comparison, catalysts obtained by *in situ* growth of cobalt sulfide on a titanium mesh ( $\text{Co}_9\text{S}_8$ –Ti) and nickel sulfide on Ni foam ( $\text{Ni}_3\text{S}_2$ –NF) were also successfully synthesized (see “Experimental section” for more details).

To reveal the morphology and microstructure features of the catalytic materials, field-emission scanning electron

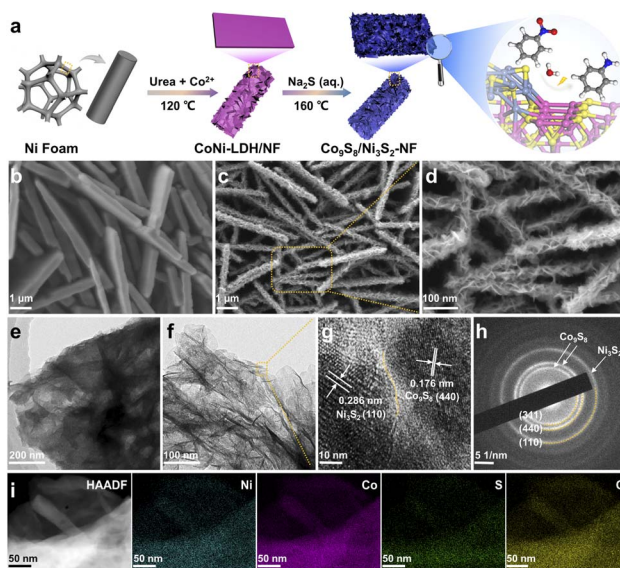


Fig. 1 (a) Schematic illustration of the formation of  $\text{Co}_9\text{S}_8/\text{Ni}_3\text{S}_2$ –NF. (b) SEM image of the CoNi-LDH/NF precursor. (c) and (d) SEM images, (e)–(g) TEM image, (h) SAED pattern, and (i) HAADF-STEM image and corresponding EDS elemental mapping of  $\text{Co}_9\text{S}_8/\text{Ni}_3\text{S}_2$ –NF.

microscopy (SEM) and transmission electron microscopy (TEM) were used. CoNi-LDH shows a smooth surface and uniform growth on Ni-foam (see Fig. 1b and S1†). The  $\text{Co}_9\text{S}_8/\text{Ni}_3\text{S}_2$ –NF exhibits an obvious hierarchical nanosheet structure (*i.e.*, nanosheets on the top of nanosheets), which implies that the sulfuration process takes place *in situ* on the CoNi-LDH/NF templates (Fig. 1c and d). Similarly, as shown in Fig. 1e and f, TEM images with different magnifications can more intuitively demonstrate the hierarchical nanosheets structure of  $\text{Co}_9\text{S}_8/\text{Ni}_3\text{S}_2$ –NF. High-resolution TEM (HRTEM) further reveals clear lattice fringes and intimate contact between  $\text{Co}_9\text{S}_8$  (440) and  $\text{Ni}_3\text{S}_2$  (110), confirming the formation of the heterojunction (see Fig. 1g). In addition, the selected area electron diffraction (SAED) pattern of  $\text{Co}_9\text{S}_8/\text{Ni}_3\text{S}_2$ –NF displays diffraction rings which can be satisfactorily ascribed to the (311) and (440) crystal planes of  $\text{Co}_9\text{S}_8$ , and the (110) crystal plane of  $\text{Ni}_3\text{S}_2$  (Fig. 1h). EDS elemental maps (Fig. 1i and S2†) show the homogeneous distribution of Co, Ni, S and O elements, further supporting the successful synthesis of  $\text{Co}_9\text{S}_8/\text{Ni}_3\text{S}_2$ –NF, and the cobalt/nickel atomic ratio is about 3.48 (Table S3†). SEM images of  $\text{Co}_9\text{S}_8$ –Ti and  $\text{Ni}_3\text{S}_2$ –NF samples indicate that the monometallic TMS is spherical, and therefore it cannot grow evenly on the substrate (Fig. S3 and S4†). Further control of hydrothermal conditions can change the structure of the CoNi-LDH/NF templates (see SEM images in Fig. S5 and S6†) and hence the morphology of the catalysts. All these results confirm that the  $\text{Co}_9\text{S}_8/\text{Ni}_3\text{S}_2$ –NF with hierarchical nanosheets was successfully prepared, presumably with exposure of more active sites that benefits the mass diffusion during NO-RR.

X-ray diffraction (XRD) patterns were obtained to verify the phase structure of the catalysts. In Fig. 2a, the XRD pattern of  $\text{Co}_9\text{S}_8/\text{Ni}_3\text{S}_2$ –NF exhibits characteristic diffraction signals ascribed to the (311) and (440) planes of  $\text{Co}_9\text{S}_8$ , as well as the



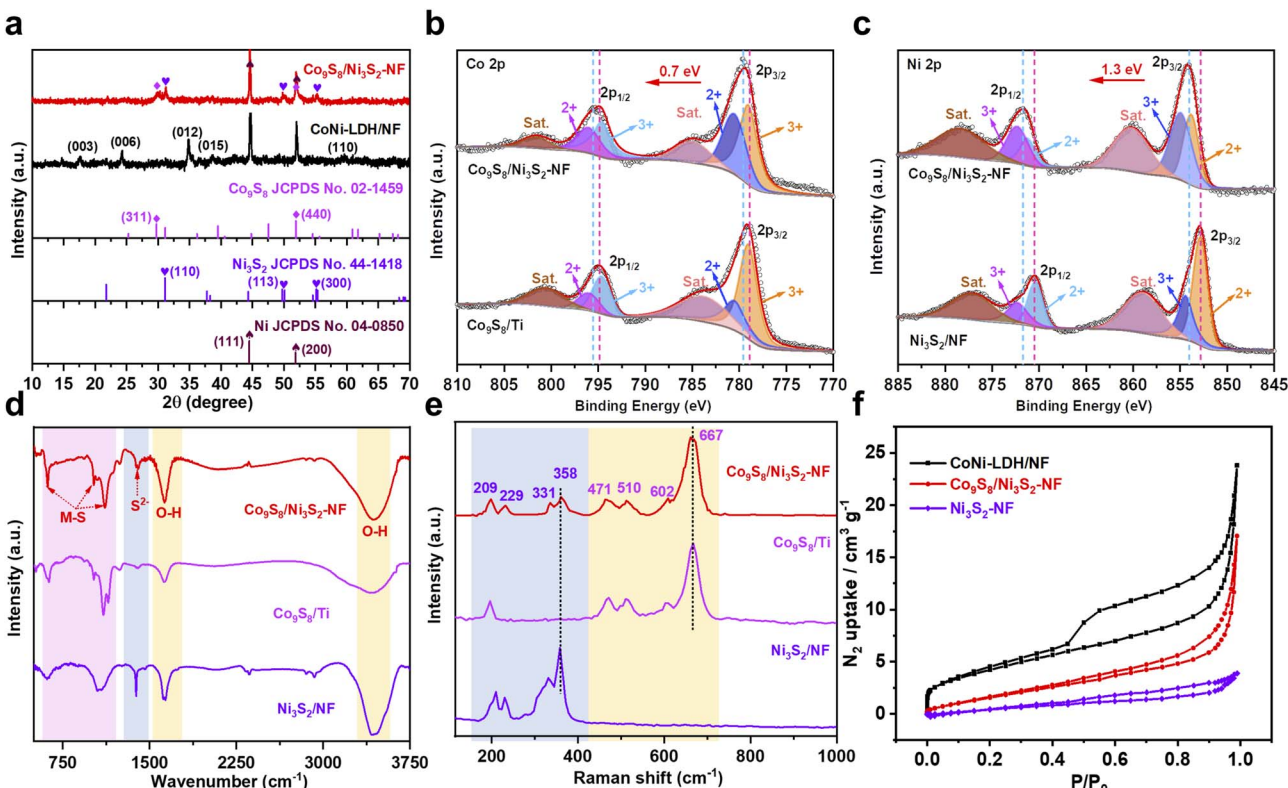


Fig. 2 (a) XRD patterns of the CoNi-LDH/NF precursor and  $\text{Co}_9\text{S}_8/\text{Ni}_3\text{S}_2$ -NF. (b) High-resolution XPS Co 2p spectra of  $\text{Co}_9\text{S}_8/\text{Ni}_3\text{S}_2$ -NF and  $\text{Co}_9\text{S}_8/\text{Ti}$ . (c) High-resolution XPS Ni 2p spectra of  $\text{Co}_9\text{S}_8/\text{Ni}_3\text{S}_2$ -NF and  $\text{Ni}_3\text{S}_2$ -NF. (d) FTIR spectra and (e) Raman spectra of  $\text{Co}_9\text{S}_8/\text{Ni}_3\text{S}_2$ -NF,  $\text{Co}_9\text{S}_8/\text{Ti}$  and  $\text{Ni}_3\text{S}_2$ -NF. (f) Nitrogen adsorption–desorption isotherms of CoNi-LDH/NF,  $\text{Ni}_3\text{S}_2$ -NF and  $\text{Co}_9\text{S}_8/\text{Ni}_3\text{S}_2$ -NF.

(110) plane of  $\text{Ni}_3\text{S}_2$  with (110) arising from the Ni foam. The XRD patterns of other samples ( $\text{Co}_9\text{S}_8$  powder,  $\text{Co}_9\text{S}_8/\text{Ti}$  and  $\text{Ni}_3\text{S}_2$ -NF) are shown in Fig. S7–S9,† indicating that all samples were successfully synthesized. Additionally, CoNi-LDH/NF shows distinct diffraction characteristic signals for the hydroxyl-like LDH phase, indicating that CoNi-LDH was successfully constructed on Ni foam.<sup>41–43</sup> X-ray photoelectron spectroscopy (XPS) was performed to obtain further insight into the chemical states of each element and the electron effect between  $\text{Co}_9\text{S}_8$  and  $\text{Ni}_3\text{S}_2$  in  $\text{Co}_9\text{S}_8/\text{Ni}_3\text{S}_2$ -NF. The XPS survey spectra in Fig. S10a† reveal the coexistence of Ni, Co, and S signals in  $\text{Co}_9\text{S}_8/\text{Ni}_3\text{S}_2$ -NF, while no signal for S is observed in CoNi-LDH/NF, and the corresponding elemental quantifications are shown in Table S4.† Fig. S10b† shows that the proportions of Co and Ni in various  $\text{Co}_9\text{S}_8/\text{Ni}_3\text{S}_2$ -NF change with the addition of Co salts for CoNi-LDH/NF production, and the optimal  $\text{Co}_9\text{S}_8/\text{Ni}_3\text{S}_2$ -NF has the highest cobalt content among the control samples. To further figure out electron transfer between  $\text{Co}_9\text{S}_8$  and  $\text{Ni}_3\text{S}_2$ , the high-resolution Co 2p, Ni 2p, and S 2p spectra were analyzed in detail.<sup>44</sup> The Co 2p spectrum of  $\text{Co}_9\text{S}_8/\text{Ni}_3\text{S}_2$ -NF was deconvoluted into six peaks including two satellite peaks, and the others observed at 780.5 and 796.0 eV for  $\text{Co}^{2+}$  as well as 779.1 and 794.6 eV for  $\text{Co}^{3+}$  are ascribed to the spin-orbit doublets Co 2p<sub>1/2</sub> and 2p<sub>3/2</sub>, respectively (Fig. 2b).<sup>45</sup> Compared to  $\text{Co}_9\text{S}_8/\text{Ti}$ , the ratio of  $\text{Co}^{3+}$  to  $\text{Co}^{2+}$  in  $\text{Co}_9\text{S}_8/\text{Ni}_3\text{S}_2$ -NF is decreased, suggesting that the average valence state of Co is decreased.<sup>33,46</sup> Moreover, the Ni 2p spectrum of  $\text{Co}_9\text{S}_8/\text{Ni}_3\text{S}_2$ -

NF (Fig. 2c) can also be deconvoluted into six subpeaks, corresponding to  $\text{Ni}^{3+}$  (854.9/872.3 eV),  $\text{Ni}^{2+}$  (853.8/871.2 eV), and two satellite peaks of Ni 2p<sub>1/2</sub> and Ni 2p<sub>3/2</sub>, severally.<sup>47</sup> Interestingly, compared to  $\text{Ni}_3\text{S}_2$ -NF, the ratio of the peak area of  $\text{Ni}^{3+}$  to  $\text{Ni}^{2+}$  for  $\text{Co}_9\text{S}_8/\text{Ni}_3\text{S}_2$ -NF is higher than that for  $\text{Ni}_3\text{S}_2$ -NF, showing that the average valence state of Ni is raised.<sup>25,48</sup> Therefore, it can be concluded that electrons transfer from  $\text{Ni}_3\text{S}_2$  to  $\text{Co}_9\text{S}_8$  through their interfaces. Moreover, the S 2p spectra in Fig. S11† demonstrate the presence of metal–sulfur bonds in  $\text{Co}_9\text{S}_8/\text{Ni}_3\text{S}_2$ -NF.<sup>40,49</sup> Besides, the XPS survey spectra of the other control samples during optimization are detailed in Fig. S12–S14.† Notably, elemental oxygen is detected in almost all materials due to the large amount of hydroxyl or  $\text{H}_2\text{O}$  molecules adsorbed on the catalyst surface during the hydrothermal reaction (Table S4†).

The Fourier transform infrared (FTIR) spectra were recorded to analyze the surface groups. Fig. 2d exhibits the FTIR spectra of  $\text{Co}_9\text{S}_8/\text{Ni}_3\text{S}_2$ -NF,  $\text{Co}_9\text{S}_8/\text{Ti}$  and  $\text{Ni}_3\text{S}_2$ -NF samples, and the two strong typical peaks at 3436 and 1631  $\text{cm}^{-1}$  are ascribed to the stretching and bending vibration of O–H of surface-adsorbed  $\text{H}_2\text{O}$  molecules.<sup>50,51</sup> Besides, the obvious peaks at 1116 and 1020  $\text{cm}^{-1}$  are attributed to the asymmetrical stretch of metal–sulfur, whereas the peak at 621  $\text{cm}^{-1}$  corresponds to symmetrical vibrations. The presence of an additional band at 1381  $\text{cm}^{-1}$  is due to the vibration of sulfide ions in the crystal in the TMS microstructures.<sup>52</sup> Furthermore, compared with single metal analogues, the characteristic peaks at 194, 459, 507, 602

and  $660\text{ cm}^{-1}$  are assigned to the vibrational modes of the  $\text{Co}_9\text{S}_8$  phase in  $\text{Co}_9\text{S}_8/\text{Ni}_3\text{S}_2\text{-NF}$ , and the peaks in the  $150\text{--}400\text{ cm}^{-1}$  region represent the phonon modes of heazlewoodite-phase  $\text{Ni}_3\text{S}_2$  (Fig. 2e).<sup>53–56</sup> In addition, the FTIR and Raman spectra of CoNi-LDH can be seen in Fig. S15 and S16,<sup>†</sup> illustrating the successful synthesis of the template.<sup>57,58</sup> The Brunauer–Emmett–Teller (BET) surface area and pore texture of  $\text{Co}_9\text{S}_8/\text{Ni}_3\text{S}_2\text{-NF}$  were analyzed using  $\text{N}_2$  adsorption–desorption measurements. Compared with  $\text{Ni}_3\text{S}_2\text{/NF}$ ,  $\text{Co}_9\text{S}_8/\text{Ni}_3\text{S}_2\text{-NF}$  results in a higher BET surface area of  $7.37\text{ m}^2\text{ g}^{-1}$  (Fig. 2f), and a higher average pore size of about  $14.32\text{ nm}$  (Fig. S17<sup>†</sup>) due to the hierarchical nanosheet structure (Fig. 2f and Table S5<sup>†</sup>).<sup>33</sup>

To explore the electrochemical NO-RR properties of the catalysts under ambient aqueous conditions, an H-type cell was constructed with a Pt plate counter electrode, an  $\text{Hg}/\text{HgO}$  reference electrode, and the self-supporting  $\text{Co}_9\text{S}_8/\text{Ni}_3\text{S}_2\text{-NF}$  as the working electrode (Fig. S18<sup>†</sup>). First, linear sweep voltammetry (LSV) curves of nitroarenes reduction and hydrogen evolution reaction (HER) were recorded in  $1.0\text{ M KOH}$  solution using 1,4-dioxane as the co-solvent. In the presence of  $\text{PhNO}_2$  (0.8 mmol),  $\text{Co}_9\text{S}_8/\text{Ni}_3\text{S}_2\text{-NF}$  exhibits the lowest onset potential ( $E_{\text{onset}}$ ) of  $0.371\text{ V}$  *versus* the reversible hydrogen electrode (RHE) compared with  $\text{Co}_9\text{S}_8\text{/Ti}$  and  $\text{Ni}_3\text{S}_2\text{/NF}$  catalysts (Fig. 3a), indicating the best NO-RR performance. Besides,  $\text{Co}_9\text{S}_8/\text{Ni}_3\text{S}_2\text{-NF}$  also has the most positive  $E_{\text{onset}}$  for the HER (Fig. 3a), which suggests that  $\text{Co}_9\text{S}_8/\text{Ni}_3\text{S}_2\text{-NF}$  is favorable for  $\text{H}_2\text{O}$  dissociation and  $\text{H}^*$  generation. Previous studies have shown that such *in*

*situ* generated  $\text{H}^*$  is beneficial for subsequent protonation reactions of  $\text{PhNO}_2$ .<sup>15</sup> In addition, the Nyquist plots from electrochemical impedance spectroscopy (EIS) show that  $\text{Co}_9\text{S}_8/\text{Ni}_3\text{S}_2\text{-NF}$  shows a much lower internal resistance and smaller charge-transfer resistance compared with the control catalysts (Fig. 3b), implying better charge transfer capability of  $\text{Co}_9\text{S}_8/\text{Ni}_3\text{S}_2\text{-NF}$ . The solution resistance ( $R_s$ ), electrode resistance ( $R_a$ ), charge transfer resistance ( $R_{\text{ct}}$ ) and constant phase element (CPE) in the equivalent circuit model (Fig. 3b, inset) were extracted by fitting the experimental results and are listed in Table S6.<sup>†</sup> The smaller  $R_{\text{ct}}$  of  $\text{Co}_9\text{S}_8/\text{Ni}_3\text{S}_2\text{-NF}$  than  $\text{Ni}_3\text{S}_2\text{/NF}$  and  $\text{Co}_9\text{S}_8\text{/Ti}$  reveals a faster charge transfer process in NO-RR.<sup>59</sup> During the catalyst optimization, LSV curves (Fig. S19<sup>†</sup>) and Nyquist plots (Fig. S20<sup>†</sup>) of all samples were also recorded. In order to confirm the intrinsic activity of NO-RR of the obtained metal sulfides, electrochemical active surface areas (ECSA) and normalized current density by ECSA were also investigated.<sup>60–62</sup> According to CV curves without faradaic processes (Fig. S21a–c<sup>†</sup>), the calculated capacitance and the ECSA are summarized in Table S7.<sup>†</sup> The ECSA of  $\text{Co}_9\text{S}_8/\text{Ni}_3\text{S}_2\text{-NF}$  is 3.0 times and 1.7 times larger than that of  $\text{Ni}_3\text{S}_2\text{/NF}$  and  $\text{Co}_9\text{S}_8\text{/Ti}$  respectively, indicating that the active sites on  $\text{Co}_9\text{S}_8/\text{Ni}_3\text{S}_2\text{-NF}$  are more accessible. Moreover, the normalized LSV curve of  $\text{Co}_9\text{S}_8/\text{Ni}_3\text{S}_2\text{-NF}$  exhibits a higher current density than  $\text{Ni}_3\text{S}_2\text{/NF}$  and  $\text{Co}_9\text{S}_8\text{/Ti}$ , showing the best intrinsic activity for NO-RR of  $\text{Co}_9\text{S}_8/\text{Ni}_3\text{S}_2\text{-NF}$  (Fig. S21e<sup>†</sup>).

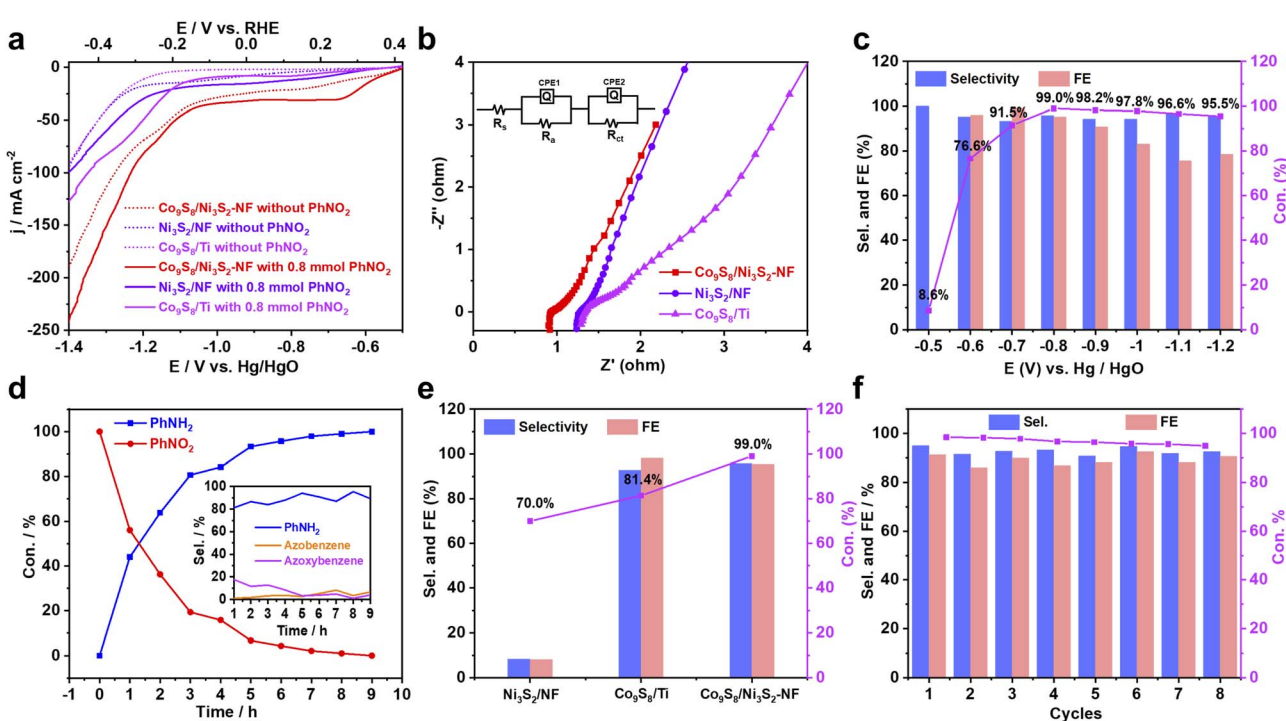


Fig. 3 (a) LSV curves of the cathode at a scan rate of  $5\text{ mV s}^{-1}$  in  $1.0\text{ M KOH}$  solution (Diox/ $\text{H}_2\text{O}$ , 2 : 5 v/v) with and without  $0.8\text{ mmol}$  of  $\text{PhNO}_2$ . (b) Nyquist plots of  $\text{Co}_9\text{S}_8/\text{Ni}_3\text{S}_2\text{-NF}$ ,  $\text{Co}_9\text{S}_8\text{/Ti}$  and  $\text{Ni}_3\text{S}_2\text{/NF}$  catalysts. (c) Potential-dependent conversion (Con.) of  $\text{PhNO}_2$ , selectivity (Sel.) and FE of  $\text{PhNH}_2$  over  $\text{Co}_9\text{S}_8/\text{Ni}_3\text{S}_2\text{-NF}$  within 8 h at  $0.121\text{ V}$  (vs. RHE). (d) Time-dependent evolution of  $\text{PhNO}_2$  and  $\text{PhNH}_2$  products over  $\text{Co}_9\text{S}_8/\text{Ni}_3\text{S}_2\text{-NF}$  (inset: selectivity (Sel.) of all products). (e) Conversion (Con.) of  $\text{PhNO}_2$ , selectivity (Sel.) and FE of  $\text{PhNH}_2$  of  $\text{Co}_9\text{S}_8/\text{Ni}_3\text{S}_2\text{-NF}$ ,  $\text{Co}_9\text{S}_8\text{/Ti}$  and  $\text{Ni}_3\text{S}_2\text{/NF}$  within 8 h at  $0.121\text{ V}$  (vs. RHE). (f) Cycle-dependent performance of transforming  $\text{PhNO}_2$  into  $\text{PhNH}_2$  over  $\text{Co}_9\text{S}_8/\text{Ni}_3\text{S}_2\text{-NF}$  within 8 cycles (8 h per cycle) at  $0.121\text{ V}$  (vs. RHE).



To explore the potential-dependence of the selectivity of  $\text{PhNH}_2$ , the electrocatalytic reduction of  $\text{PhNO}_2$  over  $\text{Co}_9\text{S}_8/\text{Ni}_3\text{S}_2$ -NF was carried out at various potentials from 0.421 to  $-0.279$  V (vs. RHE) (Fig. 3c) by gas chromatography (GC) (Fig. S22–S23†). The wide  $E_{\text{onset}}$  gap between NO-RR and HER indicates efficient and highly selective reduction of  $\text{PhNO}_2$  to  $\text{PhNH}_2$  on the  $\text{Co}_9\text{S}_8/\text{Ni}_3\text{S}_2$ -NF electrode at different potentials from 0.321 to  $-0.079$  V (vs. RHE). Specifically, the optimal catalytic performances for  $\text{PhNO}_2$  to  $\text{PhNH}_2$  were achieved at 0.121 V (vs. RHE) with up to 99.0% conversion, 96.0% selectivity and 95.3% faradaic efficiency (FE) (Table S8†). Nevertheless,  $\text{PhNO}_2$  cannot be reduced at potentials higher than 0.421 V (vs. RHE) and demonstrates low conversion and FE at potentials

more negative than  $-0.079$  V (vs. RHE) due to the dominant HER. In Fig. 3d, time-dependent transformations reveal that  $\text{PhNO}_2$  is almost completely converted to  $\text{PhNH}_2$  within  $\sim 8$  h at 0.121 V (vs. RHE), and the corresponding selectivity of NO-RR is depicted in the inset of Fig. 3d. By contrast, lower conversion and selectivity are obtained over  $\text{Co}_9\text{S}_8/\text{Ti}$  and  $\text{Ni}_3\text{S}_2/\text{NF}$  cathodes at 0.121 V (vs. RHE), showing the promotion effect of the  $\text{Co}_9\text{S}_8/\text{Ni}_3\text{S}_2$  heterojunction in NO-RR (Fig. 3e). The other control catalysts were also evaluated to verify the more significant electrochemical performance of  $\text{Co}_9\text{S}_8/\text{Ni}_3\text{S}_2$ -NF (Fig. S24†).

Furthermore, the electrocatalytic stability of  $\text{PhNO}_2$  reduction is assessed over  $\text{Co}_9\text{S}_8/\text{Ni}_3\text{S}_2$ -NF. After 8 cycles (8 h per cycle) of electrolysis at 0.121 V vs. RHE,  $\text{Co}_9\text{S}_8/\text{Ni}_3\text{S}_2$ -NF maintained

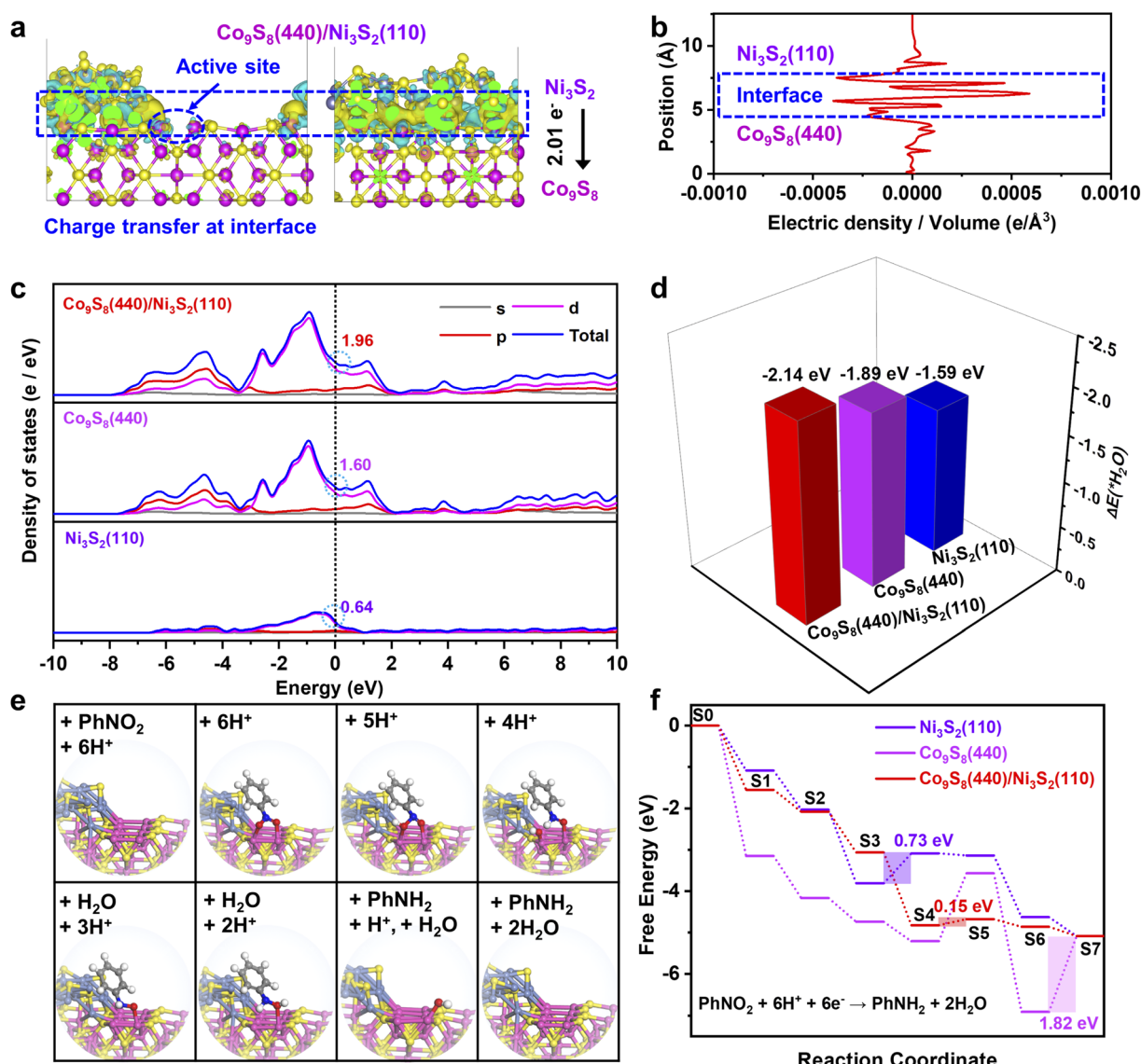


Fig. 4 (a) The front and left views of calculated charge density difference of the  $\text{Co}_9\text{S}_8/\text{Ni}_3\text{S}_2$ -NF heterostructure. (b) The corresponding radial distribution function over  $\text{Co}_9\text{S}_8/\text{Ni}_3\text{S}_2$ -NF. (c) The calculated projected density of states on  $\text{Co}_9\text{S}_8/\text{Ni}_3\text{S}_2$ -NF,  $\text{Co}_9\text{S}_8/\text{Ti}$  and  $\text{Ni}_3\text{S}_2/\text{NF}$  systems. (d) Calculated  $\text{H}_2\text{O}$  adsorption energy. (e) The catalytic pathway on the  $\text{Co}_9\text{S}_8/\text{Ni}_3\text{S}_2$  surface. (f) The computational energy profile of the optimized intermediates for  $\text{Co}_9\text{S}_8$  (440),  $\text{Ni}_3\text{S}_2$  (110), and the  $\text{Co}_9\text{S}_8$  (440)/ $\text{Ni}_3\text{S}_2$  (110) heterojunction. The fuchsia, caesous, yellow, gray, blue, red, and white spheres represent the Co, Ni, S, C, N, O and H atoms, respectively. The yellow and green regions represent electron accumulation and depletion, respectively.

high selectivity and FE for  $\text{PhNO}_2$  to  $\text{PhNH}_2$  conversion (Fig. 3f and Table S9†). Furthermore, the current efficiency and Nyquist plots are almost consistent with the starting cycle (Fig. S25†). Negligible changes were discovered by further SEM, TEM, XRD and XPS characterization, implying the excellent durability of the  $\text{Co}_9\text{S}_8/\text{Ni}_3\text{S}_2$ -NF cathode for NO-RR (Fig. S26–S28 and Tables S10, S11†). All these electrochemical results demonstrate that  $\text{Co}_9\text{S}_8/\text{Ni}_3\text{S}_2$ -NF shows excellent catalytic activity and promising cycle stability for application in the electrocatalytic conversion of  $\text{PhNO}_2$  for  $\text{PhNH}_2$  production.

To understand the underlying origin of the excellent activity of the  $\text{Co}_9\text{S}_8/\text{Ni}_3\text{S}_2$ -NF heterostructure, density functional theory (DFT) calculations were further employed.<sup>2,16,63,64</sup> According to the HRTEM and XRD results,  $\text{Co}_9\text{S}_8$  (440) and  $\text{Ni}_3\text{S}_2$  (110) lattice planes are preferentially exposed in  $\text{Co}_9\text{S}_8/\text{Ni}_3\text{S}_2$ -NF, and thus the models of the  $\text{Co}_9\text{S}_8$  (440),  $\text{Ni}_3\text{S}_2$  (110), and  $\text{Co}_9\text{S}_8$  (440)/ $\text{Ni}_3\text{S}_2$  (110) heterojunction surfaces were optimized (Fig. S29†). To evaluate the electronic interaction between  $\text{Co}_9\text{S}_8$  and  $\text{Ni}_3\text{S}_2$ , the calculated charge density difference within the  $\text{Co}_9\text{S}_8/\text{Ni}_3\text{S}_2$  heterojunction was analyzed. As displayed in Fig. 4a, charge density difference for the  $\text{Co}_9\text{S}_8/\text{Ni}_3\text{S}_2$  model (front and left views) clearly shows a significant charge rearrangement occurring at the interface of  $\text{Co}_9\text{S}_8/\text{Ni}_3\text{S}_2$ .<sup>35</sup> Additionally, electron accumulation is also observed on the Co atoms close the  $\text{Co}_9\text{S}_8/\text{Ni}_3\text{S}_2$  interface (marked as a blue cycle) due to electron transfer (2.01 e<sup>−</sup>) from  $\text{Ni}_3\text{S}_2$  to  $\text{Co}_9\text{S}_8$ , which was consistent with the XPS and Raman results. Such electron transfer at the  $\text{Co}_9\text{S}_8/\text{Ni}_3\text{S}_2$  interface is more directly manifested in the corresponding radial distribution function (Fig. 4b). Furthermore, the calculated projected density of states reveals that the  $\text{Co}_9\text{S}_8/\text{Ni}_3\text{S}_2$  heterostructure has a higher electron density of 1.96 at the Fermi level than single  $\text{Co}_9\text{S}_8$  (1.60) and  $\text{Ni}_3\text{S}_2$  (0.64) (Fig. 4c), which can facilitate electron transfer.<sup>65</sup> Notably, all three models present no band gap crossing the Fermi level, indicating that the  $\text{Co}_9\text{S}_8/\text{Ni}_3\text{S}_2$  heterostructure preserves the metallic nature of  $\text{Ni}_3\text{S}_2$  and  $\text{Co}_9\text{S}_8$  with high conductivity.

The adsorption energies of  $\text{H}_2\text{O}$  ( $\Delta E_{\text{H}_2\text{O}}$ ) and the energy profile of the  $\text{PhNO}_2$  reduction were further studied. As shown in Fig. 4d, the  $\text{Co}_9\text{S}_8/\text{Ni}_3\text{S}_2$  heterojunction has a more negative  $\Delta E_{\text{H}_2\text{O}}$  value of  $-2.14$  eV than  $\text{Co}_9\text{S}_8$  ( $-1.89$  eV) and  $\text{Ni}_3\text{S}_2$  ( $-1.59$  eV), which implies effective  $\text{H}_2\text{O}$  activation for  $\text{H}^*$  generation on the  $\text{Co}_9\text{S}_8/\text{Ni}_3\text{S}_2$  interface.<sup>23</sup> This calculation result is in line with the HER experimental measurements in alkaline medium (Fig. S19†), and the *in situ* formed active  $\text{H}^*$  at the interface will participate in the transfer hydrogenation of  $\text{PhNO}_2$ .

According to the structural optimization of intermediates in the aqueous electrochemical reduction of  $\text{PhNO}_2$ , the corresponding energy profile of  $\text{PhNO}_2$  hydrogenation on the  $\text{Co}_9\text{S}_8/\text{Ni}_3\text{S}_2$  surface along the pathway was calculated. The catalytic cycle is displayed in Fig. 4e, and specific elementary steps are as follows: (i)  $\text{PhNO}_2 + * \rightarrow \text{PhNO}_2^*$ ; (ii)  $\text{PhNO}_2^* + \text{H} + \text{e}^- \rightarrow \text{PhNOOH}^*$ ; (iii)  $\text{PhNOOH}^* + \text{H} + \text{e}^- \rightarrow \text{PhNHO}^*\text{OH}$ ; (iv)  $\text{PhNHO}^*\text{OH} + \text{H} + \text{e}^- \rightarrow \text{PhNHO}^* + \text{H}_2\text{O}$ ; (v)  $\text{PhNHO}^* + \text{H} + \text{e}^- \rightarrow \text{PhNHOH}^*$ ; (vi)  $\text{PhNHOH}^* + \text{H} + \text{e}^- \rightarrow \text{PhNH}_2 + \text{OH}^*$ ; (vii)  $\text{OH}^* + \text{H} + \text{e}^- \rightarrow \text{H}_2\text{O}$ , in which \* represents the adsorption site. Notably, the  $\text{PhNO}_2$  molecule will

spontaneously adsorb on two Co atoms close to the  $\text{Co}_9\text{S}_8/\text{Ni}_3\text{S}_2$  interface, such a diatomic metal-site adsorption mechanism has also been reported in thermal catalysis under high pressure.<sup>63</sup> For comparison, both  $\text{Co}_9\text{S}_8$  and  $\text{Ni}_3\text{S}_2$  were also considered, and the corresponding mechanism process is shown in Fig. S30†.

Fig. 4f exhibits the computational energy profiles of the optimized intermediates for  $\text{Co}_9\text{S}_8$  (440),  $\text{Ni}_3\text{S}_2$  (110), and the  $\text{Co}_9\text{S}_8$  (440)/ $\text{Ni}_3\text{S}_2$  (110) heterojunction at  $U = 1.23$  V *vs.* the reversible hydrogen electrode.<sup>66</sup> Logically,  $\text{Co}_9\text{S}_8/\text{Ni}_3\text{S}_2$  exhibits a lower energy absorption of 0.15 eV on the rate determining step (RDS) compared to  $\text{Co}_9\text{S}_8$  of 1.82 eV and  $\text{Ni}_3\text{S}_2$  of 0.73 eV, conforming to the unique catalytic activities of  $\text{Co}_9\text{S}_8/\text{Ni}_3\text{S}_2$ -NF again. Compared with pure  $\text{Co}_9\text{S}_8$ , the  $\text{Co}_9\text{S}_8/\text{Ni}_3\text{S}_2$  model is more beneficial to the desorption of OH ( $\text{S}6 \rightarrow \text{S}7$ ), which is because the  $\text{Co}_9\text{S}_8/\text{Ni}_3\text{S}_2$  interface breaks the charge symmetry of two Co atom sites (Fig. 4a).

Hence, the OH intermediate is prone to adhere to one Co atom at the  $\text{Co}_9\text{S}_8/\text{Ni}_3\text{S}_2$  surface, but it exhibits strong bridging adsorption on symmetric two cobalt atoms at the  $\text{Co}_9\text{S}_8$  surface (Fig. 4e and S29†). Overall, calculations demonstrate that the  $\text{Co}_9\text{S}_8/\text{Ni}_3\text{S}_2$  heterojunction is beneficial for activation of  $\text{H}_2\text{O}$ , reducing the energy barrier of subsequent  $\text{PhNO}_2$  hydrogenation and facilitating electron transfer at interfaces.

Table 1 Selective electroreduction of various substituted nitroarenes over the  $\text{Co}_9\text{S}_8/\text{Ni}_3\text{S}_2$ -NF cathode<sup>a</sup>

Entry	Reactant	Product	Con. (%)	Sel. (%)	FE (%)
1			100.0	97.5	96.9
2			96.3	100.0	96.2
3			93.6	95.4	96.0
4			100.0	97.1	98.1
5			100.0	99.3	97.0
6			100.0	97.6	96.3
7			97.7	97.9	95.0
8			100.0	99.5	90.2
9			99.5	99.9	98.1
10			97.1	98.5	96.4
11			79.4	98.3	84.0

<sup>a</sup> Reaction conditions: nitro substrates (0.8 mmol),  $\text{Co}_9\text{S}_8/\text{Ni}_3\text{S}_2$ -NF (working area:  $1 \text{ cm}^2$ ), 1.0 M KOH solution (Diox/ $\text{H}_2\text{O}$ , 2 : 5 v/v), room temperature,  $-0.421 \sim -0.279$  V (*vs.* RHE), 8 h. The conversion (Con.), selectivity (Sel.) and faradaic efficiency (FE) were determined by gas chromatography.



On the basis of DFT results, ultraviolet photoelectron spectroscopy (UPS) measurements were performed to gain further insights into interfacial electron transfer capacity. Fig. S31<sup>†</sup> shows that the work functions of  $\text{Co}_9\text{S}_8/\text{Ni}_3\text{S}_2\text{-NF}$ ,  $\text{Co}_9\text{S}_8/\text{Ti}$  and  $\text{Ni}_3\text{S}_2/\text{NF}$  catalysts were calculated to be 6.77, 6.28 and 5.89 eV, severally. The low work function of  $\text{Co}_9\text{S}_8/\text{Ni}_3\text{S}_2\text{-NF}$  indicates a rapid electron donation capacity from the catalyst surface to the adsorbed nitro groups.<sup>67,68</sup> Therefore, theoretical calculations and experiments together show that the construction of the  $\text{Co}_9\text{S}_8/\text{Ni}_3\text{S}_2$  heterojunction facilitates the efficient reduction of  $\text{PhNO}_2$  to  $\text{PhNH}_2$ .

The general applicability of the electrochemical selective hydrogenation of nitroarenes towards aminoarenes was extended with excellent performance over the  $\text{Co}_9\text{S}_8/\text{Ni}_3\text{S}_2\text{-NF}$  cathode (Table 1).<sup>2,69</sup> Obviously, a series of functionalized aminoarenes with electro-donating groups of  $-\text{OCH}_3$  and  $-\text{OH}$ , and electron withdrawing groups of  $-\text{Cl}$  and  $-\text{F}$  on the *ortho*, *meta* or *para* positions can be obtained in excellent yields (entries 1–6). Nitroarenes with other fragile  $-\text{Br}$  and  $-\text{COCH}_3$  groups were also successfully converted with excellent yields (entries 7–10). Due to the two hexatomic rings of the 5-nitroquinoline substrate, the difficult adsorption of 5-nitroquinoline on the catalyst leads to a low conversion of NO-RR compared to other functionalized aminoarenes (entry 11). Overall, these results signify that the potential applicability of  $\text{Co}_9\text{S}_8/\text{Ni}_3\text{S}_2\text{-NF}$  provides a good opportunity for subsequent generation of more complex molecules, which are challenging in traditional synthesis methods.

## Conclusions

In summary, self-supporting hierarchical nanosheets composed of  $\text{Co}_9\text{S}_8/\text{Ni}_3\text{S}_2$  heterojunctions were fabricated *via* an *in situ* sulphuration strategy using layered double hydroxide as a self-sacrificing template. Because of the integration of plentiful active  $\text{Co}_9\text{S}_8/\text{Ni}_3\text{S}_2$  interfaces, open nanostructure, and high conductivity, the as-prepared  $\text{Co}_9\text{S}_8/\text{Ni}_3\text{S}_2\text{-NF}$  shows outstanding NO-RR performance in alkaline aqueous medium. Both the experimental results and theoretical calculations reveal electron transfer from  $\text{Ni}_3\text{S}_2$  to  $\text{Co}_9\text{S}_8$ , which is identified by electron redistribution at interfaces. For this reason, the  $\text{Co}_9\text{S}_8/\text{Ni}_3\text{S}_2$  heterojunction is more conducive to the adsorption of  $\text{H}_2\text{O}$  and  $\text{PhNO}_2$  for the formation of  $\text{H}^*$  and further protonation of  $\text{PhNO}_2$ . Furthermore, interfacial charge transfer can break the symmetry of two active Co sites at the  $\text{Co}_9\text{S}_8/\text{Ni}_3\text{S}_2$  interface to change the strong bridging adsorption of OH on Co sites, which markedly reduces the energy barrier. In addition,  $\text{Co}_9\text{S}_8/\text{Ni}_3\text{S}_2\text{-NF}$  also exhibits good functional group tolerance and excellent cycling stability for electrocatalytic NO-RR. This work reveals the electrocatalytic mechanism for NO-RR on metal sulfide-based heterojunctions, and reflects the advantage and great potential of interfacial engineering for green synthesis.

## Data availability

All data associated with this article have been included in the main text and ESI.<sup>†</sup>

## Author contributions

Y. C., M. D., and P. Z. conceived the concept and supervised the project. K. Y. contributed to valuable guidance and comments. X. W. and L. L. searched the literature and performed the synthesis, characterization and electrochemical experiments. G. X. and M. S. assisted with the HR-TEM testing and data analysis. Y. W. assisted with the XRD testing and data analysis. The manuscript was written through contributions of all authors.

## Conflicts of interest

There are no conflicts to declare.

## Acknowledgements

The authors acknowledge financial support from the National Natural Science Foundation of China (52073137, 22172075, and 92156024), the Education Department Science and Technology Research Foundation of Jiangxi Province (GJJ210318), the Natural Science Foundation of Jiangxi Province (20212BAB213018, 20203BDH80W011, and 20212BAB214028), and the Thousand Talents Plan of Jiangxi Province (jxsq2019102002).

## References

- 1 K. M. R. V. Jagadeesh, A. S. Alshammary, H. Neumann, M.-M. Pohl, J. Radnik and M. Beller, *Science*, 2017, **358**, 326–332.
- 2 J. L. Liang, Q. Q. Song, J. H. Wu, Q. Lei, J. Li, W. Zhang, Z. M. Huang, T. X. Kang, H. Xu, P. Wang, X. T. Zhou, P. K. Wong, H. M. Li, X. M. Meng, Z. F. Jiang and C. S. Lee, *ACS Nano*, 2022, **16**, 4152–4161.
- 3 K.-Y. Zhang, Z.-Y. Gu, E. H. Ang, J.-Z. Guo, X.-T. Wang, Y. Wang and X.-L. Wu, *Mater. Today*, 2022, **54**, 189–201.
- 4 J. Li, S. Song, Y. Long, L. Wu, X. Wang, Y. Xing, R. Jin, X. Liu and H. Zhang, *Adv. Mater.*, 2018, **30**, 1704416.
- 5 V. Babel and B. L. Hiran, *Catal. Lett.*, 2020, **150**, 1865–1869.
- 6 Y. Xie, X. Shang, D. Liu, H. Zhao, Y. Gu, Z. Zhang and X. Wang, *Appl. Catal., B*, 2019, **259**, 118087.
- 7 J. Liu, R. Ye, J. Shi, H. Wang, L. Wang, P. Jian and D. Wang, *Chem. Eng. J.*, 2021, **419**, 129640.
- 8 D. Formenti, F. Ferretti, F. K. Scharnagl and M. Beller, *Chem. Rev.*, 2018, **119**, 2611–2680.
- 9 S. Doherty, J. G. Knight, T. Backhouse, R. J. Summers, E. Abood, W. Simpson, W. Paget, R. A. Bourne, T. W. Chamberlain, R. Stones, K. R. J. Lovelock, J. M. Seymour, M. A. Isaacs, C. Hardacre, H. Daly and N. H. Rees, *ACS Catal.*, 2019, **9**, 4777–4791.
- 10 F. Tong, X. Liang, F. Ma, X. Bao, Z. Wang, Y. Liu, P. Wang, H. Cheng, Y. Dai, B. Huang and Z. Zheng, *ACS Catal.*, 2021, **11**, 3801–3809.
- 11 G. Portillo Perez and M.-J. Dumont, *Chem. Eng. J.*, 2020, **382**, 122766.
- 12 H. Wei, X. Liu, A. Wang, L. Zhang, B. Qiao, X. Yang, Y. Huang, S. Miao, J. Liu and T. Zhang, *Nat. Commun.*, 2014, **5**, 5634.



13 X. Chong, C. Liu, Y. Huang, C. Huang and B. Zhang, *Natl. Sci. Rev.*, 2020, **7**, 285–295.

14 C. Tang, Y. Zheng, M. Jaroniec and S. Z. Qiao, *Angew. Chem., Int. Ed.*, 2021, **60**, 19572–19590.

15 Y. Zhao, C. Liu, C. Wang, X. Chong and B. Zhang, *CCS Chem.*, 2021, **3**, 507–515.

16 M. Jin, Y. Liu, X. Zhang, J. Wang, S. Zhang, G. Wang, Y. Zhang, H. Yin, H. Zhang and H. Zhao, *Appl. Catal., B*, 2021, **298**, 120545.

17 X. Huang, Q. Zhang, J. Lin, K. Harms and E. Meggers, *Nat. Catal.*, 2018, **2**, 34–40.

18 Y. Yuan and A. Lei, *Acc. Chem. Res.*, 2019, **52**, 3309–3324.

19 B. K. Peters, K. X. Rodriguez, S. H. Reisberg, S. B. Beil, D. P. Hickey, Y. Kawamata, M. Collins, J. Starr, L. Chen, S. Udyavara, K. Klunder, T. J. Gorey, S. L. Anderson, M. Neurock, S. D. Minteer and P. S. Baran, *Science*, 2019, **363**, 838–845.

20 P. Xiong and H.-C. Xu, *Acc. Chem. Res.*, 2019, **52**, 3339–3350.

21 D. Carvajal, R. Arcas, C. A. Mesa, S. Giménez, F. Fabregat-Santiago and E. Mas-Marzá, *Adv. Sustainable Syst.*, 2022, **6**, 2100367.

22 K. Iwase, N. Fujinami, K. Hashimoto, K. Kamiya and S. Nakanishi, *Chem. Lett.*, 2018, **47**, 304–307.

23 G. Yang, Y. Jiao, H. Yan, Y. Xie, A. Wu, X. Dong, D. Guo, C. Tian and H. Fu, *Adv. Mater.*, 2020, **32**, 2000455.

24 Y. Wu, Y. Liu, G.-D. Li, X. Zou, X. Lian, D. Wang, L. Sun, T. Asefa and X. Zou, *Nano Energy*, 2017, **35**, 161–170.

25 Y. Sun, J. Wu, Z. Zhang, Q. Liao, S. Zhang, X. Wang, Y. Xie, K. Ma, Z. Kang and Y. Zhang, *Energy Environ. Sci.*, 2022, **15**, 633–644.

26 A. Sivanantham, P. Ganesan and S. Shanmugam, *Adv. Funct. Mater.*, 2016, **26**, 4661–4672.

27 J. Sun, H. Xue, N. Guo, T. Song, Y. r. Hao, J. Sun, J. Zhang and Q. Wang, *Angew. Chem., Int. Ed.*, 2021, **60**, 19435–19441.

28 S. Chandrasekaran, L. Yao, L. Deng, C. Bowen, Y. Zhang, S. Chen, Z. Lin, F. Peng and P. Zhang, *Chem. Soc. Rev.*, 2019, **48**, 4178–4280.

29 Z. Zhang, L. Bian, H. Tian, Y. Liu, Y. Bando, Y. Yamauchi and Z. L. Wang, *Small*, 2022, **18**, 2107450.

30 Z. L. Wang, J. Choi, M. Xu, X. Hao, H. Zhang, Z. Jiang, M. Zuo, J. Kim, W. Zhou, X. Meng, Q. Yu, Z. Sun, S. Wei, J. Ye, G. G. Wallace, D. L. Officer and Y. Yamauchi, *ChemSusChem*, 2020, **13**, 929–937.

31 Y. Sun, H. Shin, F. Wang, B. Tian, C.-W. Chiang, S. Liu, X. Li, Y. Wang, L. Tang, W. A. Goddard and M. Ding, *J. Am. Chem. Soc.*, 2022, **144**, 15185–15192.

32 Y.-T. Liao, V. C. Nguyen, N. Ishiguro, A. P. Young, C.-K. Tsung and K. C. W. Wu, *Appl. Catal., B*, 2020, **270**, 118805.

33 J. Zhang, J. Qian, J. Ran, P. Xi, L. Yang and D. Gao, *ACS Catal.*, 2020, **10**, 12376–12384.

34 W. Fang, H. Hu, T. Jiang, G. Li and M. Wu, *Carbon*, 2019, **146**, 476–485.

35 S. Wang, L. Zhao, J. Li, X. Tian, X. Wu and L. Feng, *J. Energy Chem.*, 2022, **66**, 483–492.

36 M. Wang, C.-L. Dong, Y.-C. Huang and S. Shen, *ACS Catal.*, 2020, **10**, 1855–1864.

37 Z. Xiong, C. Hu, X. Luo, W. Zhou, Z. Jiang, Y. Yang, T. Yu, W. Lei and C. Yuan, *Nano Lett.*, 2021, **21**, 10486–10493.

38 B. Yan, D. Krishnamurthy, C. H. Hendon, S. Deshpande, Y. Surendranath and V. Viswanathan, *Joule*, 2017, **1**, 600–612.

39 Y. Yan, S. Ding, X. Zhou, Q. Hu, Y. Feng, Q. Zheng, D. Lin and X. Wei, *J. Alloys Compd.*, 2021, **867**, 158941.

40 S. Adhikari, Y. Kwon and D.-H. Kim, *Chem. Eng. J.*, 2020, **402**, 126192.

41 X. Guan, M. Huang, L. Yang, G. Wang and X. Guan, *Chem. Eng. J.*, 2019, **372**, 151–162.

42 M. Zhang, Y. Liu, B. Liu, Z. Chen, H. Xu and K. Yan, *ACS Catal.*, 2020, **10**, 5179–5189.

43 R. Zhang, Z. Xue, J. Qin, M. Sawangphruk, X. Zhang and R. Liu, *J. Energy Chem.*, 2020, **50**, 143–153.

44 W. He, C. Wang, H. Li, X. Deng, X. Xu and T. Zhai, *Adv. Energy Mater.*, 2017, **7**, 1700983.

45 Y. Wang, J. Huang, Y. Xiao, Z. Peng, K. Yuan, L. Tan and Y. Chen, *Carbon*, 2019, **147**, 146–153.

46 K. Shah, R. Dai, M. Mateen, Z. Hassan, Z. Zhuang, C. Liu, M. Israr, W. C. Cheong, B. Hu, R. Tu, C. Zhang, X. Chen, Q. Peng, C. Chen and Y. Li, *Angew. Chem., Int. Ed.*, 2021, **134**, e202114951.

47 K. Zhang, Y. Wei, J. Huang, Y. Xiao, W. Yang, T. Hu, K. Yuan and Y. Chen, *Sci. China Mater.*, 2020, **63**, 1898–1909.

48 Y. Lu, C.-L. Dong, Y.-C. Huang, Y. Zou, Y. Liu, Y. Li, N. Zhang, W. Chen, L. Zhou, H. Lin and S. Wang, *Sci. China: Chem.*, 2020, **63**, 980–986.

49 M. Verma, L. Sinha and P. M. Shirage, *J. Mater. Sci.: Mater. Electron.*, 2021, **32**, 12292–12307.

50 D. Jiang, H. Liang, W. Yang, Y. Liu, X. Cao, J. Zhang, C. Li, J. Liu and J. J. Gooding, *Carbon*, 2019, **146**, 557–567.

51 J. Zhao, L. Song, X. Liang and Z. Zhao, *Inorg. Chem. Commun.*, 2019, **107**, 107469.

52 S. Surendran, K. Vijaya Sankar, L. John Berchmans and R. Kalai Selvan, *Mater. Sci. Semicond. Process.*, 2015, **33**, 16–23.

53 W. Li, Y. Li, H. Fu, G. Yang, Q. Zhang, S. Chen and F. Peng, *Chem. Eng. J.*, 2020, **381**, 122683.

54 L. Zeng, K. Sun, X. Wang, Y. Liu, Y. Pan, Z. Liu, D. Cao, Y. Song, S. Liu and C. Liu, *Nano Energy*, 2018, **51**, 26–36.

55 C. Xia, P. Li, A. N. Gandi, U. Schwingenschlögl and H. N. Alshareef, *Chem. Mater.*, 2015, **27**, 6482–6485.

56 H. Wang, Y. Yang, Q. Li, W. Lu, J. Ning, Y. Zhong, Z. Zhang and Y. Hu, *Sci. China Mater.*, 2020, **64**, 840–851.

57 T.-J. Wang, X. Liu, Y. Li, F. Li, Z. Deng and Y. Chen, *Nano Res.*, 2019, **13**, 79–85.

58 Y. Feng, X. Wang, J. Huang, P. Dong, J. Ji, J. Li, L. Cao, L. Feng, P. Jin and C. Wang, *Chem. Eng. J.*, 2020, **390**, 124525.

59 P. Liu, J. Yan, J. Mao, J. Li, D. Liang and W. Song, *J. Mater. Chem. A*, 2020, **8**, 11435–11441.

60 L. Li, S. Huang, R. Cao, K. Yuan, C. Lu, B. Huang, X. Tang, T. Hu, X. Zhuang and Y. Chen, *Small*, 2021, **18**, 2105387.

61 S. He, H. Du, K. Wang, Q. Liu, J. Sun, Y. Liu, Z. Du, L. Xie, W. Ai and W. Huang, *Chem. Commun.*, 2020, **56**, 5548–5551.

62 Y. Liu, Q. Li, R. Si, G.-D. Li, W. Li, D.-P. Liu, D. Wang, L. Sun, Y. Zhang and X. Zou, *Adv. Mater.*, 2017, **29**, 1606200.



63 S. Tian, B. Wang, W. Gong, Z. He, Q. Xu, W. Chen, Q. Zhang, Y. Zhu, J. Yang, Q. Fu, C. Chen, Y. Bu, L. Gu, X. Sun, H. Zhao, D. Wang and Y. Li, *Nat. Commun.*, 2021, **12**, 3181.

64 Y. Gu, A. Wu, L. Wang, D. Wang, H. Yan, P. Yu, Y. Xie, C. Tian, F. Sun and H. Fu, *J. Mater. Chem. A*, 2020, **8**, 4807–4815.

65 J. Wu, R. Zhao, H. Xiang, C. Yang, W. Zhong, C. Zhang, Q. Zhang, X. Li and N. Yang, *Appl. Catal., B*, 2021, **292**, 120200.

66 Y. Li, R. Cao, L. Li, X. Tang, T. Chu, B. Huang, K. Yuan and Y. Chen, *Small*, 2020, **16**, 1906735.

67 Z. Wu, Y. Zhang, L. Li, Y. Zhao, Y. Shen, S. Wang and G. Shao, *J. Mater. Chem. A*, 2020, **8**, 23248–23256.

68 B. Ni, R. Chen, L. Wu, P. Sun and T. Chen, *Sci. China Mater.*, 2020, **64**, 1159–1172.

69 M. Niakan and Z. Asadi, *Catal. Lett.*, 2019, **149**, 2234–2246.

